Nitrogen-doped carbon nanotubes with encapsulated Fe nanoparticles as efficient oxygen reduction catalyst for alkaline membrane direct ethanol fuel cells

Muhammad Rauf,[a,c] Rongrong Chen[b], Qiang Wang[b], Yu-Cheng Wang[a], Zhi-You Zhou[a,*]

a. State Key Laboratory of Physical Chemistry of Solid Surfaces, Collaborative Innovation Center of Chemistry for Energy Materials, College of Chemistry and Chemical Engineering, Xiamen University, Xiamen, 361005, China.

b. Richard G. Lugar Center for Renewable Energy, Indiana University-Purdue University, Indianapolis, IN, 46202, United States

c. College of Chemistry and Environmental Engineering, Shenzhen University, Shenzhen, Guangdong 518060, PR China.

* Corresponding author. Tel: +86-592-2180181; Email: zhouzy@xmu.edu.cn (Zhi-You Zhou)

Abstract

Exploring low-cost and highly efficient non-precious metal electrocatalysts toward oxygen reduction reaction is crucial for the development of fuel cells. Herein, we report the synthesis of bamboo-like N-doped carbon nanotubes with encapsulated Fe-nanoparticles through high-temperature pyrolysis of multiple nitrogen complex consisting of benzoguanamine, cyanuric acid, and melamine. As-prepared catalyst exhibits high catalytic activity for oxygen reduction with onset potential of 1.10 V and half-wave potential of 0.93 V, as well as low H_2O_2 yield (< 1%) in alkaline medium.

This is the author's manuscript of the article published in final edited form as:
Rauf, M., Chen, R., Wang, Q., Wang, Y.-C., & Zhou, Z.-Y. (2017). Nitrogen-doped carbon nanotubes with encapsulated Fe nanoparticles as efficient oxygen reduction catalyst for alkaline membrane direct ethanol fuel cells. Carbon. https://doi.org/10.1016/j.carbon.2017.09.093

The mass activity of the catalyst at 1.0 V (0.58 A g^{-1}) can reach 43% of state-of-the-art commercial Pt/C. This catalyst also exhibits high durability and ethanol tolerance. When it was applied in alkaline membrane direct ethanol fuel cell, the peak power density could reach to 64 mW cm^{-2}, indicating its attractive application prospect in fuel cells.

1. Introduction

Oxygen reduction reaction (ORR) is an important reaction in various electrochemical energy conversion and storage devices such as fuel cells and metal-air batteries. The kinetics of ORR is very sluggish, and has to be accelerated by Pt-based electrocatalysts. However, the high cost and low abundance of Pt severely impede the large-scale applications of above electrochemical energy devices. It is critical to design efficient ORR electrocatalysts based on non-precious metals (NPM) [1-6]. Recently, carbon-based nanomaterials with heteroatom doping (e.g., Fe, N, S, P and F) have been considered as promising NPM catalysts to replace Pt-based electrocatalysts for ORR [3, 7-12]. Among them, nitrogen-doped carbon nanotubes (CNTs), especially CNTs with encapsulated Fe nanoparticles have attracted great interests [2, 3, 13-16]. For example, Deng et al reported that Fe encapsulated within pod-like CNTs had shown considerably high catalytic activity for ORR [15]. The catalytic activity was attributed to the electron transfer from Fe nanoparticles to the CNTs leading to a decreased local work function on the carbon surface. Meanwhile, the carbon shells avoid the direct contact of Fe nanoparticles with harsh environments including acid medium, oxygen, and sulfur contaminations, so that, the catalyst has a rather high

stability [15]. Nevertheless, the catalytic activity and stability of carbon-based NPM electrocatalysts do not satisfy the requirement of practical applications yet, especially in acidic proton exchange membrane fuel cell (PEMFCs) due to metal active sites leaching, protonation of nitrogen active species (e.g., pyridinic N), and carbonaceous corrosion [17-20]. In contrast, carbon-based NPM catalysts exhibit considerably high ORR activity and stability in alkaline medium [2, 21-26]. However, their applications are limited by the poor performance of alkaline membrane, as well as slow mass transfer in catalyst micropores where most of activity sites are located. Recently, substantial progress has made in alkaline anion exchange membrane (AEM) [27-29], therefore, exploring the applications of carbon-based NPM catalysts in AEM fuel cells has attracted great interests.

In direct alcohol fuel cells (DAFCs), noble metal-based ORR catalysts are susceptible to alcohol crossover from anode to cathode, resulting in the decrease in cell voltage and fuel efficiency. In this respect, NMP catalysts are desirable, because they are insensitive to alcohols. That is, fuel crossover cannot reduce the ORR performance of NMP catalysts [23, 30]. In addition, the Pt loading of DAFCs is usually one order of magnitude higher than that of H_2-O_2 PEMFCs. It is economically significant to replace Pt-based catalysts with NPM catalysts for ORR in the DAFCs [31, 32].

In this study, we synthesized nitrogen-doped carbon nanotubes with encapsulated Fe nanoparticles by using multiple nitrogen complex as nitrogen precursor, and $FeCl_3$ as an iron source through high-temperature pyrolysis. The multiple nitrogen complex

was prepared from benzoguanamine (Bg), cyanuric acid (CA) and melamine (M). As-synthesized catalyst has bamboo-like structure with large diameter (50-200 nm), and high mesopore surface area (556 m^2 g^{-1}) that facilitates the accessibility of active-site and mass transfer. As a result, the catalyst exhibits high ORR activity (0.58 A g^{-1}@1.0V) and durability, as well as high ethanol tolerance in alkaline solution. When the catalyst was applied in alkaline AEM direct ethanol fuel cell (DEFC), the peak power density could be as high as 64 mW cm^{-2}.

2. Experimental

2.1 Chemicals and materials

Benzoguanamine (99%), cyanuric acid (99%), and melamine (99%) were purchased from Alfa Aesar. Pt/C (20 wt% Pt, Alfa Aesar), sulfuric acid (suprapur 96.0%, Merck), Ketjenblack EC600J (KJ600, Akzo Nobel), Nafion (D520, 5%, Dupont) and sodium hydroxide (NaOH, 98.0%, Sigma-Aldrich), were used as received. High purity Ar (99.999%), O_2 (99.998%) and N_2 (99.99%) were purchased from Linde Industrial Gases. The water used throughout all the experiments was ultrapure water (18.2 MΩ) purified through a Millipore system.

2.2 Synthesis of (Bg-CA-M)-Fe/N/C catalyst

The preparation process of the (Bg-CA-M)-Fe/N/C catalyst is illustrated in Fig. 1. The multiple nitrogen complex was synthesized according to previously reported method [33]. In a typical synthesis, benzoguanamine (0.74 g, 3.95 mmol), cynuric acid (1 g, 7.75 mmol), melamine (0.5 g, 3.96 mmol) and water (50 ml) were charged to a 100 ml flask with a magnetic stir bar. Then the reactants were mixed for 4 h under

stirring on a magnetic plate. After that, white multiple nitrogen complex was precipitated by filtration over a Buchner funnel and washed with excess of water. The resulting white powder was dried at 60 °C over night in a vacuum oven. Finally, the dry white powder of multiple nitrogen complex (0.5 g) was mixed with $FeCl_3 \cdot 6H_2O$ (0.25 g) in tetrahydrofuran by ultra-sonication for 20 minutes. After that, KJ600 carbon black (0.15 g) was added into the mixture of multiple nitrogen complex and $FeCl_3$, and further sonicated for 20 minutes. The mixture was stirred on a magnetic plate to obtain a homogeneous mixture at room temperature for 4 h. Then, the solvent was removed through rotary evaporator and further dried in vacuum oven at 60 °C for 8 h. The resulting dried catalyst precursor was subjected to the 1^{st} heat treatment at different temperature (700, 800 and 900°C) under argon atmosphere for 1 h. The pyrolyzed sample was then subjected to acid leaching in 0.1 M H_2SO_4 at 80°C for 7 h to remove unstable and inactive species (e.g., Fe_3C and FeS). After the acid leaching, the sample was washed thoroughly with de-ionized water followed by centrifugation and dried in vacuum oven at 60 °C. Second heat treatment was performed at same temperature for 3 h under argon gas. The final catalyst was labelled as (Bg-CA-M)-Fe/N/C. For comparison, we also synthesized the catalysts from different combination of nitrogen precursors by similar processes, e.g., (Bg-CA)-Fe/N/C was synthesized from Bg and CA.

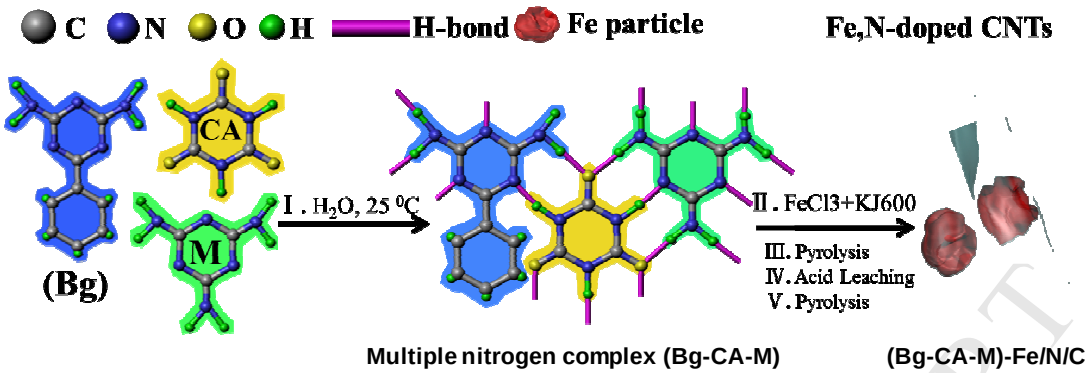

Fig. 1: Illustration of the synthesis of multiple nitrogen complex and (Bg-CA-M)-Fe/N/C catalyst. Bg: Benzoguanamine; CA: Cynuric acid; M: Melamine

2.3 Characterization

The morphologies and structure of (Bg-CA-M)-Fe/N/C catalyst were investigated by scanning electron microscope (SEM, Hitachi S-4800) and transmission electron microscope (TEM, JEM-2100 at 200 kV) and X-ray diffraction (XRD, Rigaku Ultima IV with Cu Kα radiation). The surface elemental composition of the catalyst was analysed through X-ray photoelectron spectroscopy (XPS, Qtac-100 LEISS-XPS instrument). Ar adsorption/desorption isotherm was tested by a Micromeritics ASAP 2020 system (USA).

2.4 Electrochemical measurements

ORR tests were carried out in a conventional three-electrode cell using CHI760D bipotentiostat connected with rotating ring-disk electrode (RRDE, Pine Inc.) in O_2-saturated 0.1 M NaOH solution. A thin graphite plate and Hg/HgO electrode were used as the counter and reference electrode, respectively. All potentials in this study refer to that of reversible hydrogen electrode (RHE) according to Eq.1:

$$E\,(\mathrm{RHE}) = E\,(\mathrm{Hg/HgO}) + 0.918\ \mathrm{V}\ldots\ldots\ldots\ldots (1)$$

A RRDE electrode with a Pt ring and a glassy carbon disk (geometric area 0.2475 cm^2) was used as working electrode to determine the ORR performance. To prepare the working electrode, the 6-10 mg catalyst, 0.45 mL water, 0.5 mL ethanol, and 50 μL 5% Nafion solution were ultrasonically mixed for 1 h to form a uniform catalyst ink. Then, 25 μL of the catalyst ink was dropped onto the polished glassy carbon electrode. The loading of the catalyst was 0.6-1.0 mg cm^2. To test ORR polarization curves, electrode potential was scanned between 0.4-1.2 V at 10 mV s^{-1}. The ring potential was fixed at 1.3 V to measure the H_2O_2 intermediate. The rotating speed was 900 rpm. Solution ohmic drop (i.e., *iR* drop) was compensated. To correct the background capacitive current, the polarization curve recorded in O_2-saturated solution was subtracted by that recorded in N_2-saturated solution.

The kinetic current (i_k) for the ORR can be derived from the experimental data using the Koutecky-Levich equation (Eq. 2):

$$\frac{1}{i} = \frac{1}{i_L} + \frac{1}{i_k} \qquad (2)$$

Where i and i_L are the measured current and diffusion limiting current, respectively. The mass activity (j_m) was calculated via the normalization of i_k with the catalyst loading on the electrode surface. The H_2O_2 yield was calculated by following equation (Eq. 3):

$$\mathrm{H_2O_2}(\%) = 200 \times \frac{I_R / N_0}{(I_R / N_0) + I_D} \qquad (3)$$

Where, I_D and I_R is the disk and ring current, respectively, and N_0 is the ring collection efficiency. The N_0 was determined to be 0.386 ± 0.002 in a solution of 5 mM

$K_4Fe(CN)_6$ + 1 M $Sr(NO_3)_2$. The H_2O_2 yield can be directly correlated with the average number of electrons (n_e) transferred per O_2 molecule through the following Eq. 4:

$$n_e = 4 - (\%\ H_2O_2)/50\% \qquad (4)$$

2.5 Fuel cell tests

Fuel cell tests were performed on 850e Scribner fuel cell system (Scribner Associates, USA). Membrane Electrode Assembly (MEAs) was constructed by hot pressing a pre-treated alkaline anion exchange membrane (A-201, purchased from Tokuyama Corp. Japan). The cathode catalyst ink was composed of 80 wt% (Bg-CA-M)-Fe/N/C (16 mg) with 20 wt% A4 anion-exchange ionomer (Tukuyama). The anode catalyst ink was composed of 16 mg 20 wt% Pd/C-homemade (80%) with Nafion solution (20%) as ionomer. Cathode or anode catalyst ink (catalyst + ionomer solution dispersing in ethanol) was sprayed on 6.25 cm^2 A201 membrane and Ni foam to form catalyst-coated membrane (ccm). The cathode diffusion layer was made by 5% PTFE-treated carbon paper. The flow rate of humidified O_2 was 300 sccm in cathode. The anode was pumped with the solution of 2 M ethanol + 1 M KOH at 2 mL min^{-1}.

3. Results and discussion

3.1 Physical characterization

Fig. 2a and 2b show the SEM and TEM images of (Bg-CA-M)-Fe/N/C sample after the 1st heat treatment at 800 ^oC. Many bamboo-like carbon nanotubes with encapsulated nanoparticles can be observed clearly. Some encapsulated nanoparticles

can survive after the acid leaching due to the protection of carbon shells. Fig. 2c and 2d show TEM images of the sample after acid leaching and the 2nd heat treatment at 800 ^{o}C (denoted as (Bg-CA-M)-Fe/N/C@800^{o}C). Clearly, the Fe-nanoparticles are preserved in carbon shells of bamboo-like CNTs. The CNTs have an outer diameter of 50-200 nm and length of 500-2000 nm. As compared with previously reported bamboo-like CNTs with the typical diameter of 10-50 nm [2, 15], the as-prepared CNTs show much large diameters. The encapsulated nanoparticles were further identified by HRTEM (Fig. 2e). The lattices space of the encapsulated nanoparticles was measured to be 0.200 nm, corresponding to (110) fringe of α-Fe. The SAED pattern (the inset of Fig. 2e) further confirms the crystalline structure of Fe. The Fe nanoparticles exist at the tips and within the compartments of bamboo-like CNTs because of Fe-catalysed growth of CNTs. These Fe nanoparticles are covered by 5-10 carbon atomic layers, which can prevent Fe nanoparticles from the direct contact with oxygen and acid, and thus avoid the corrosion. Raman spectroscopic test indicates that (Bg-CA-M)-Fe/N/C@800^{o}C has relative low graphitization degree with the intensity ratio of D band to G band (I_D/I_G) of 1.11 (Fig. S1). This may be caused by high level of doping heteroatoms (e.g., N and O) and defects, as well as the coexistence of carbon black that comes from the precursor. The high concentration of defects and doping heteroatoms will facilitate the ORR activity.

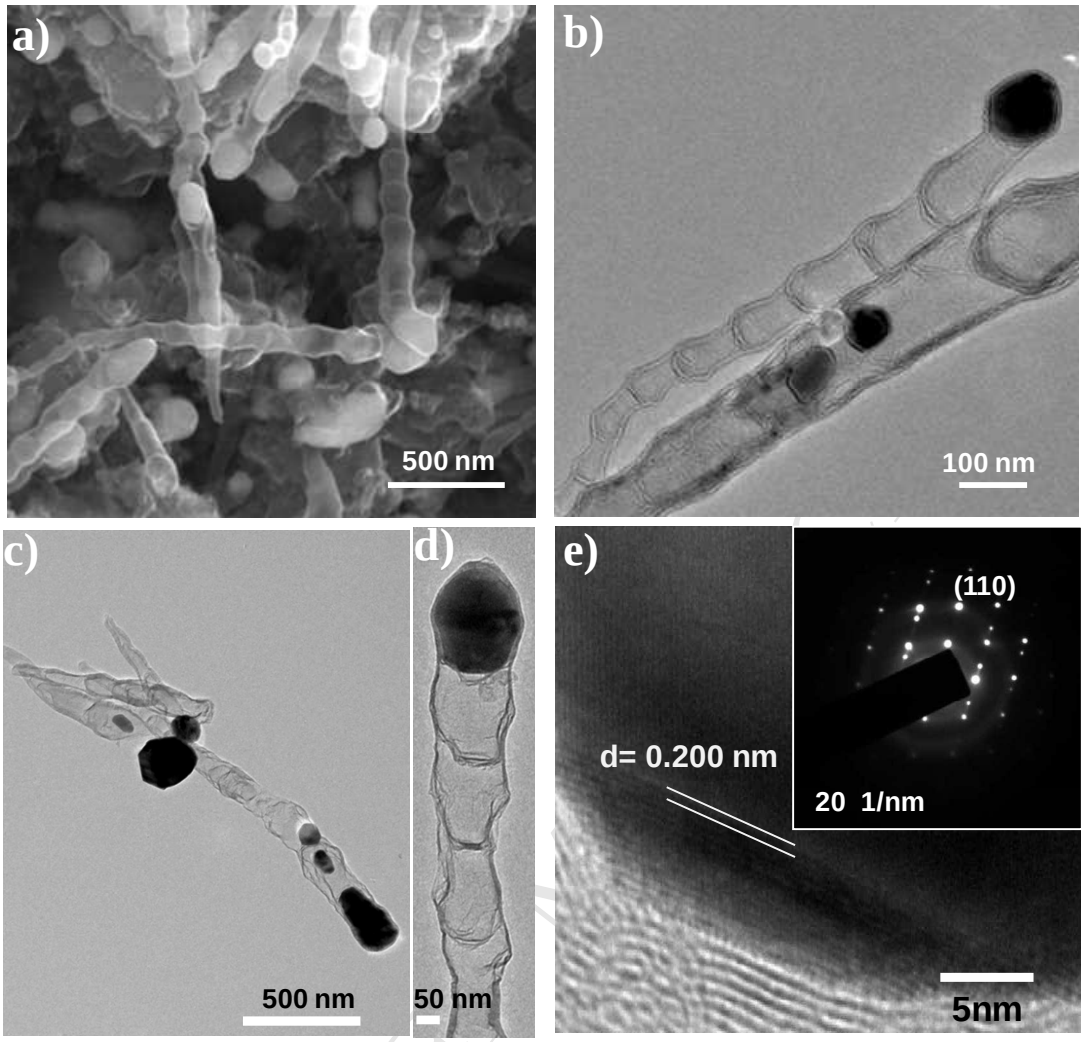

Fig. 2 Morphology characterization of (Bg-CA-M)-Fe/N/C catalyst. (a) SEM and (b) TEM images of the sample just after the 1st heat treatment at 800 °C. (c, d) TEM and HRTEM images of final (Bg-CA-M)-Fe/N/C@800°C catalyst after acid leaching and the 2nd heat treatment. (e) HR-TEM image of encapsulated Fe particle. The inset is the corresponding SAED pattern.

Crystalline structure of (Bg-CA-M)-Fe/N/C@800°C was further characterized by XRD (Fig. 3a). Two broad diffraction peaks centring at 26.2° and 43° correspond to the diffractions of the (002) and (100) faces of the graphitic framework,

respectively. The diffraction peaks at 44.7°, 65.0° and 82.3° indicate the presence of α-Fe (PDF#89-7194) in the (Bg-CA-M)-Fe/N/C@800^{o}C. The 44.7° diffraction corresponds to the lattice space of 0.202 nm, which is well consistent with the HRTEM observation (Fig. 2e). In addition, there are some weak peaks about the FeC (PDF#23-0298) and Fe_3O_4 (PDF#03-0863).

The porous structure of the (Bg-CA-M)-Fe/N/C@800°C catalyst was investigated by Ar adsorption-desorption isotherm, as demonstrated in Fig. 3b. The Brunauer-Emmett-Teller (BET) surface area was determined to be 578 $m^2 g^{-1}$. The *t*-plot analysis indicates that the catalyst has large external surface area of 556 $m^2 g^{-1}$, but small micropore area of 22 $m^2 g^{-1}$. The isotherm exhibits a type-IV curve with a distinct capillary condensation step at a relative pressure of 0.35-0.8, which can be attributed the mesoporous structure. The pore-size distribution was determined from the adsorption branch data by the Horvath-Kawazoe (HK) method for micropores (< 2 nm) and the Barret-Joyner-Halenda (BJH) method for mesopores (> 2 nm), as inset in Fig. 3b. High external surface area and abundant mesopores of the catalyst can facilitate the accessibility of reactants for ORR.

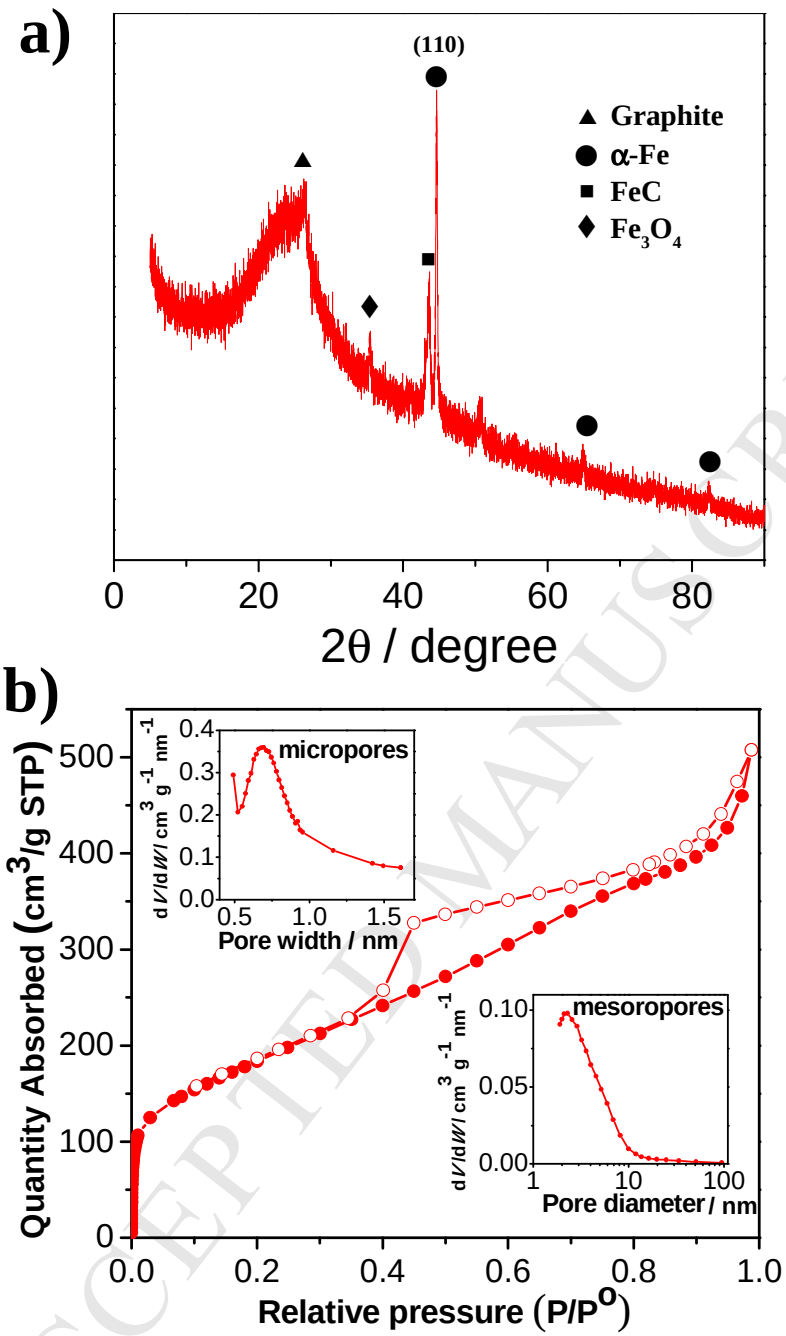

Fig. 3 XRD (a) and Ar adsorption-desorption isotherm (b) of (Bg-CA-M)-Fe/N/C@800^{o}C. Pore-size distribution was inset in (b).

3.2 ORR performance

The ORR performance of (Bg-CA-M)-Fe/NC catalysts were tested in O_2-saturated 0.1 M NaOH solution by the RRDE. For comparison, Pt/C (20 wt % Pt)

catalyst was also tested under similar conditions. We firstly monitored the ORR performance of (Bg-CA-M)-Fe/N/C at different synthetic steps (Fig. S2). Before heat treatment, the sample had little ORR activity. After 1st heat treatment (HT1), considerable ORR activity could be observed. Acid leaching could lower the ORR activity, but after 2nd heat treatment (HT2), the ORR activity was enhanced significantly, much higher than that of HT1. Active nitrogen species in NPM catalysts are formed during the heat treatment, so that the pyrolysis temperature is an important parameter [34]. To achieve the best performance, we optimized the pyrolysis temperature from 700 to 900 ^{o}C. The BET surface area of the samples slightly increased with increasing pyrolysis temperature (Fig. S3). The samples prepared at 700 ^{o}C and 800 ^{o}C contained considerable Fe-encapsulated carbon nanotubes, while that prepared at 900 ^{o}C mainly consisted of porous carbon nanoparticles (Fig. S4). Fig. 4a displays the ORR polarization curves of (Bg-CA-M)-Fe/N/C prepared at different temperature (700, 800, and 900°C), as well as Pt/C catalyst. The highest ORR activity was observed at 800 °C, in terms of high onset potential (ca. 1.10 V) and half-wave potential (ca. 0.93 V). For Pt/C reference catalyst, the onset and half-wave potentials ($E_{1/2}$) are 1.04 and 0.907 V, respectively.

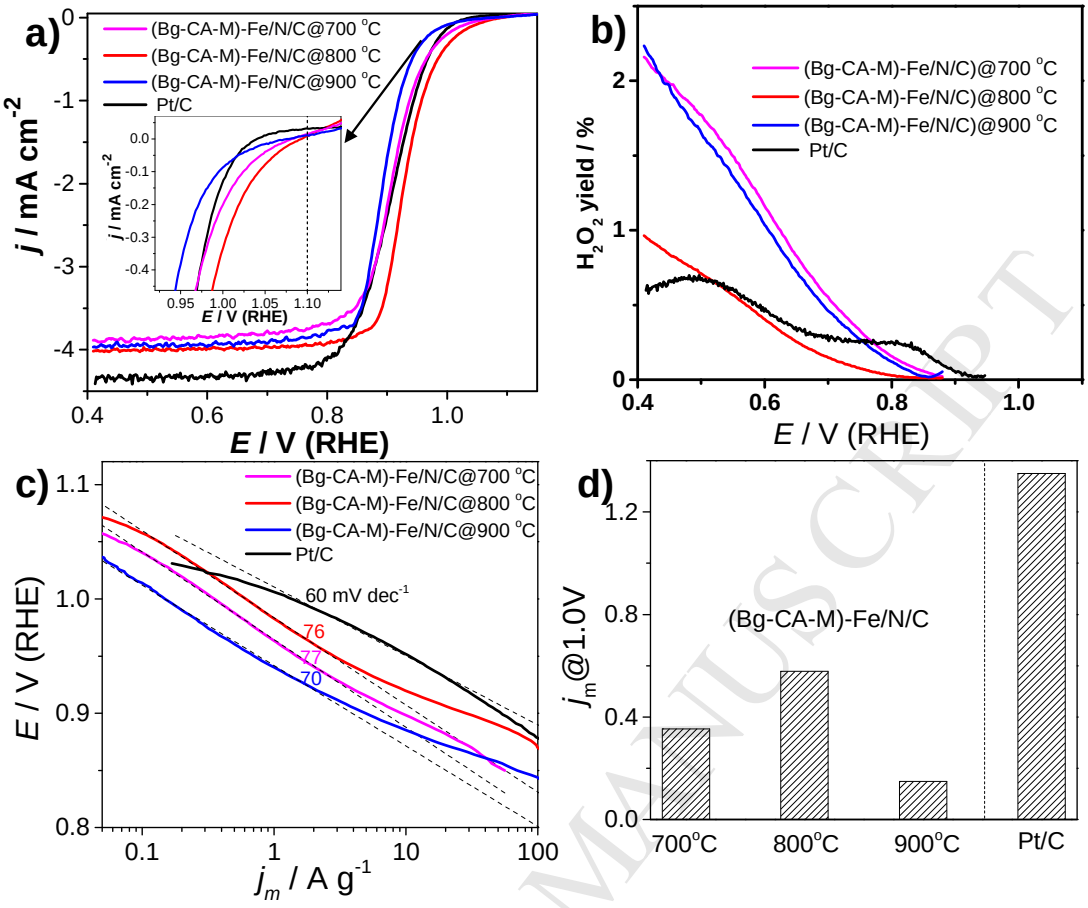

Fig. 4 ORR polarization curves (a) and H_2O_2 yield (b) of (Bg-CA-M)-Fe/N/C catalysts prepared at 700-900 °C, as well as commercial Pt/C (20 wt%) catalyst in O_2-saturated 0.1 M NaOH. The inset is the enlarged curves near 1.0 V. (Bg-CA-M)-Fe/N/C catalyst loading: 0.60 mg cm^{-2}; Pt/C loading: 0.10 mgcm^{-2} (or 20 μg Pt cm^{-2}); Rotating speed: 900 rpm; scan rate: 10 mV s^{-1}. (c) Tafel plots of the above catalysts for ORR. (d) Comparison of ORR mass activity at 1.0 V.

To further evaluate the catalytic activity, we calculated the mass activity (j_m) based on Koutecky−Levich equation (Eq. 2). The determined kinetic current was then normalized by the catalyst loading (0.6 mg cm^{-2}) to obtain the j_m. Fig. 4c illustrates the Tafel plot (E~log$^{j}_{m}$) of the (Bg-CA-M)-Fe/N/C and Pt/C catalysts. The Tafel slopes of (Bg-CA-M)-Fe/N/C catalysts slightly decrease from 77 to 70 mV dec^{-1} as

the pyrolysis temperature increased from 700 to 900 ^{o}C. These values are slightly larger than that of Pt/C (60 mV dec^{-1}). Fig. 4d shows the comparison of mass activity of the above catalysts. The mass activities of (Bg-CA-M)-Fe/N/C@800°C catalyst at 1.0 V is 0.58 A g^{-1}, reaching 43% of the Pt/C (1.35 A g_{cat}^{-1}). Note that the mass activity at 0.90 V usually calculated in the literature cannot be measured precisely in this study, because the current at 0.90 V is close to the diffusion limiting current. The $E_{1/2}$ and ORR mass activity of (Bg-CA-M)-Fe/N/C@800°C catalyst are also considerably higher than those of Fe-encapsulated or CNT-based Fe/N/C catalysts reported recently (Table S1) [2, 35, 36].

H_2O_2 yield is also an important parameter for ORR catalysts. Fig. 4b depicts the H_2O_2 yield of (Bg-CA-M)-Fe/N/C samples. The (Bg-CA-M)-Fe/N/C@800°C catalyst shows the lowest H_2O_2 yield, less than 1% in the whole potential region. This value is even lower than that of the Pt/C catalyst in the potential region of 0.50-0.90 V. The average electrons transfer number (n_e) per O_2 molecule was calculated to be over 3.98, according to the Eq. 3. Such high value of n_e indicates that ORR processes follow four electron-transfer mechanism on the (Bg-CA-M)-Fe/N/C@800°C. Low H_2O_2 yield will benefit the stability of the catalyst, because H_2O_2 can produce highly corrosive ·OH radical. As for the other two (Bg-CA-M)-Fe/N/C samples (700^{o}C and 900^{o}C), their H_2O_2 yields are about double to that of (Bg-CA-M)-Fe/N/C@800°C.

To better understand the effect of pyrolysis temperature on the ORR performance, we carried out XPS test to determine the near-surface composition and element chemical state. As shown in Fig. 5a, the (Bg-CA-M)-Fe/N/C catalysts mainly

contained C, N, O, and Fe elements. The weight content of the above elements is inset in Fig. 5a. As the pyrolysis temperature increases, the carbon weight content increases from 80.7% to 93.6 %, at the expense of lowering the doping level of N, O, and Fe. For example, nitrogen weight content decreases from 6.3% to 1.7% as the pyrolysis temperature increase from 700 to 900 ^{o}C. The chemical states of N element are very important for ORR performance. Fig. 5b shows the high-resolution N1s XPS. The elevated temperature facilitates the formation of active nitrogen species and graphitization, [19] but it also reduces the doped nitrogen content. It has been proposed that nitrogen species of pyrolysis samples include pyridinic N (398.8 ± 0.2 eV), Fe-N (399.6± 0.2 eV), pyrrolic N (400 ± 0.2 eV), graphitic N (401± 0.2 eV), and oxidized nitrogen (402± 0.3 eV) [37, 38]. However, we found that it is difficult to correlate the ORR activity with one of N species since the low-temperature sample (i.e., 700 ^{o}C) has shown low ORR activity, but very high nitrogen content, even through peak deconvolution.

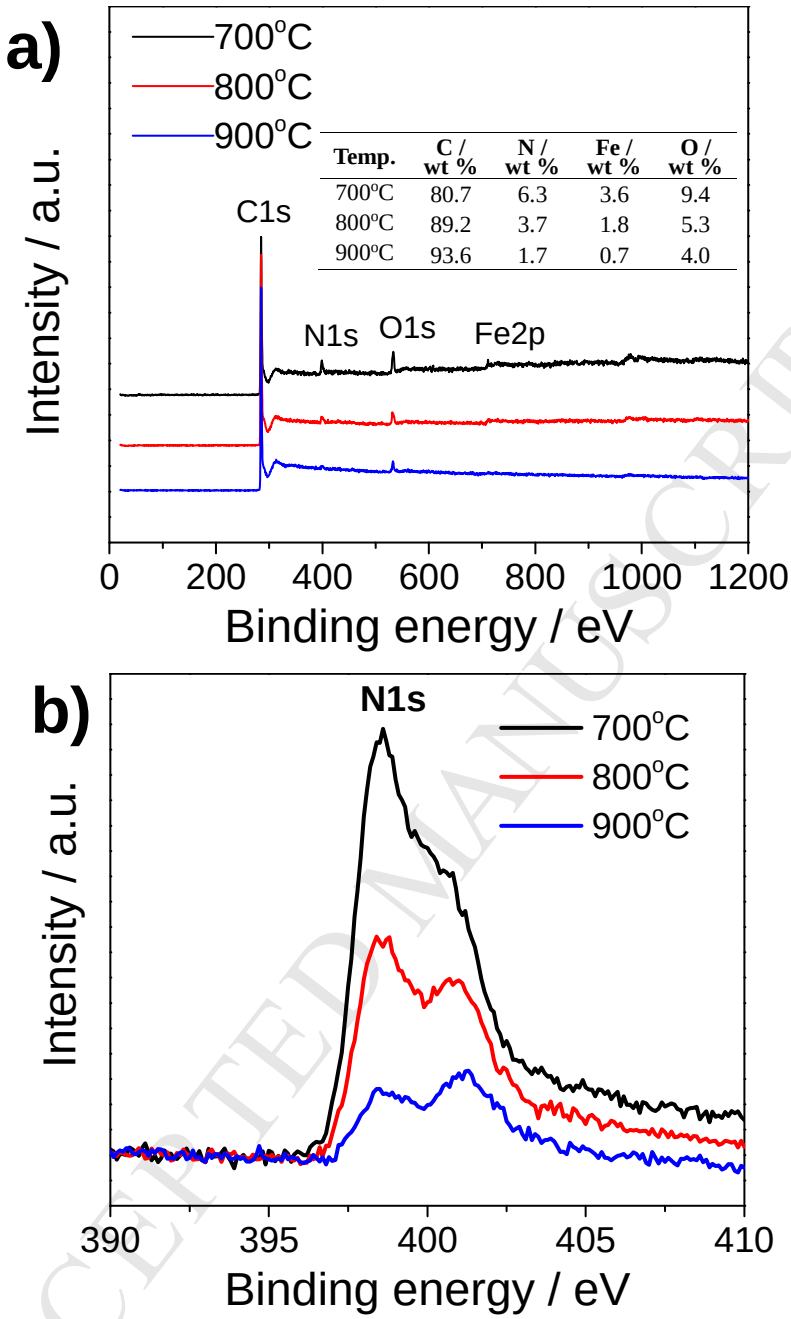

Fig. 5 XPS of (Bg-CA-M)-Fe/N/C catalysts prepared at 700-900 °C. (a) Survey spectra; (b) High-resolution N1s spectra. The weight content of C, N, Fe, and O, determined from correspongding high-resolved spectra, was inset in (a).

3.3 Effect of nitrogen precursors

(Bg-CA-M)-Fe/N/C catalyst was prepared from the multiple nitrogen complex of

Bg, CA, and M, and showed the morphology of Fe-nanoparticles encapsulated carbon nanotubes. We found such combination of nitrogen precursors (Bg + CA + M) is necessary for the formation of nanotube morphology and high ORR performance. For comparison, we synthesized with a series of catalysts with different composition of nitrogen precursors, and evaluated their ORR performance. The pyrolysis temperature was fixed at 800 ^{o}C. The synthesized catalysts included (Bg)-Fe/N/C, (CA)-Fe/N/C, (M)-Fe/N/C, (Bg-CA)-Fe/N/C, (Bg-M)-Fe/N/C, and (CA-M)-Fe/N/C.

Fig. 6a displays the ORR polarization curves of the catalysts prepared from different nitrogen precursors. Clearly, the (Bg-CA-M)-Fe/N/C@800°C exhibits the best ORR performance. We calculated the mass activity of the catalysts at 0.95 V, and compared them through a histogram (Fig. 6b). The catalytic activity decreases in the order of (Bg-CA-M) > (Bg-M) > (Bg) > (Bg-CA) > (CA-M) > (M) > (CA). It is obvious that among three nitrogen precursors, the Bg is the most important for high ORR catalytic activity. We further measured the TEM images of the above catalysts. As shown in Fig. 7, none of them have the CNT structure with encapsulated Fe-nanoparticles except the (Bg-CA-M)-Fe/N/C. The formation mechanism of CNT structure from ternary Bg-CA-M nitrogen precursor is not clear yet, and needs further investigation.

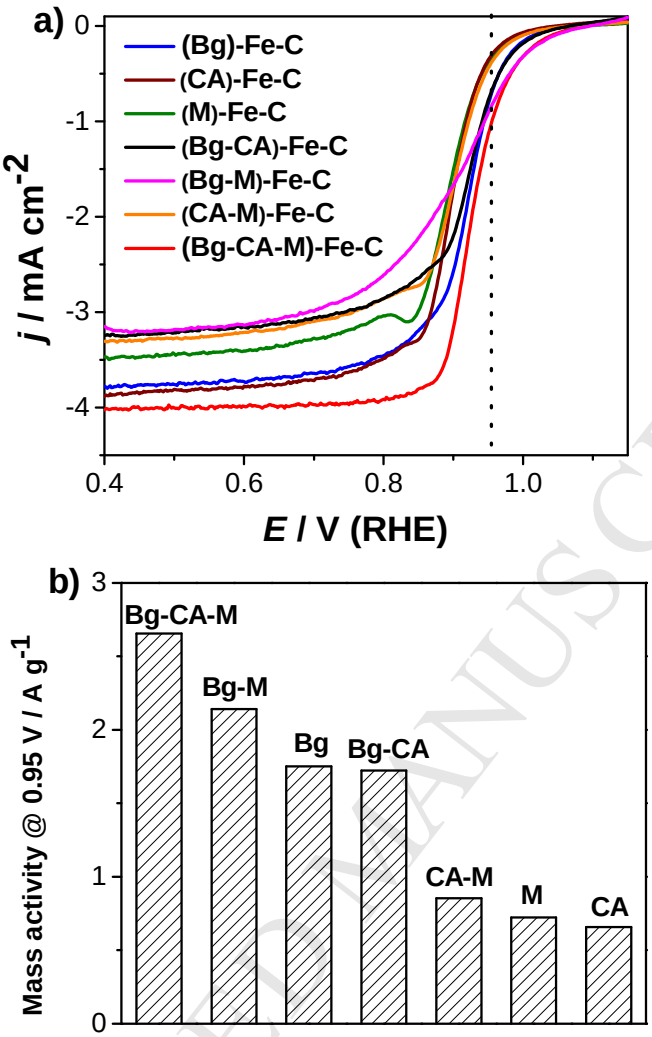

Fig. 6 (a) ORR polarization curves of the catalysts prepared from different combinations of nitrogen precursors. (b) Comparison of ORR mass activity at 0.95 V for different catalysts.

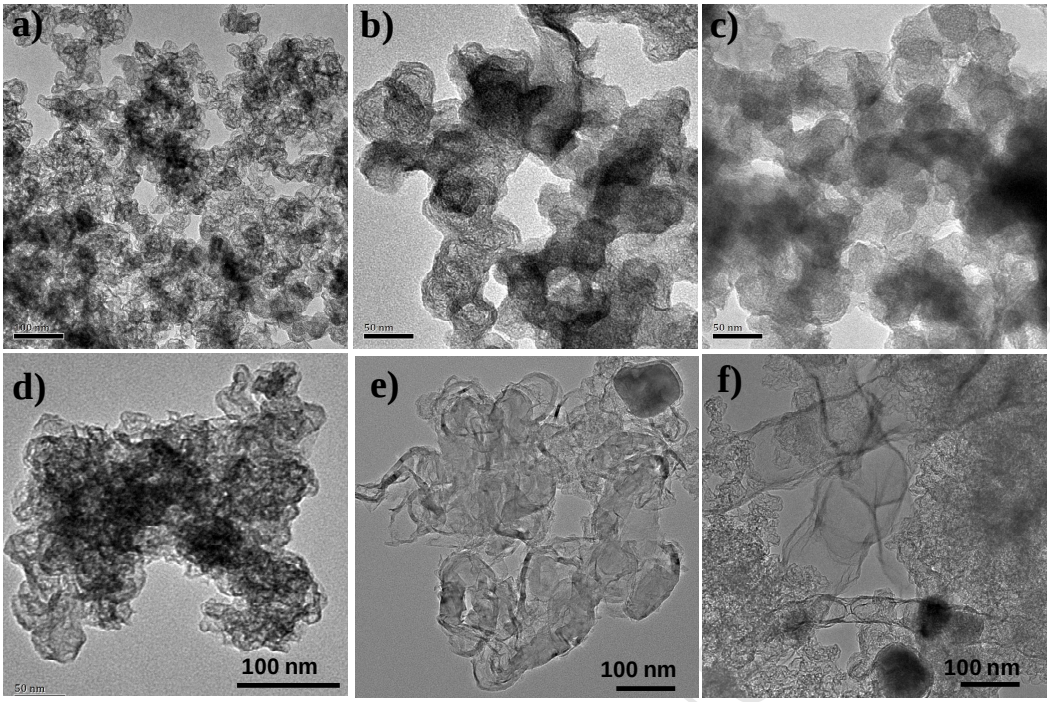

Fig. 7 TEM images of the catalysts prepared from different combinations of nitrogen precursors: (a) (Bg)-Fe/N/C@800°C; (b) (CA)-Fe/N/C@800°C; (c) (M)-Fe/N/C@800°C; (d) (Bg-M)-Fe/N/C@800°C; (e) (M-CA)-Fe/N/C@800°C; (f) (Bg-CA)-Fe/N/C@800°C.

3.4 Stability and alcohol tolerance

The stability and the resistance to alcohol crossover effect are two important parameters of the electrocatalysts for practical application in direct alcohol fuel cell. The stability of the catalyst was firstly tested by potential cycling between 0.6 and 1.0 V at 50 mV s^{-1} in O_2-saturated 0.1 M NaOH. As presented in Fig. 8a, after 10,000 potential cycles, (Bg-CA-M)-Fe/N/C@800°C just shows a small negative shift in $E_{1/2}$ by 12 mV, which is significantly lower than that of commercial Pt/C catalyst (56 mV). Furthermore, the stability was determined at constant potential of 0.80 V in

O_2-saturated 0.1 M NaOH solution at 900 rpm. The (Bg-CA-M)-Fe/N/C@800°C lost 29% of initial activity after the 100 h test (Fig. 8b). In contrast, the Pt/C catalyst degraded the same activity (-29%) just within 3 h. Such quick degradation of Pt/C performance may be attributed to the formation of Pt oxide at such high potential of 0.80 V. The above two tests clearly show that (Bg-CA-M)-Fe/N/C@800°C catalyst has high stability under alkaline ORR condition.

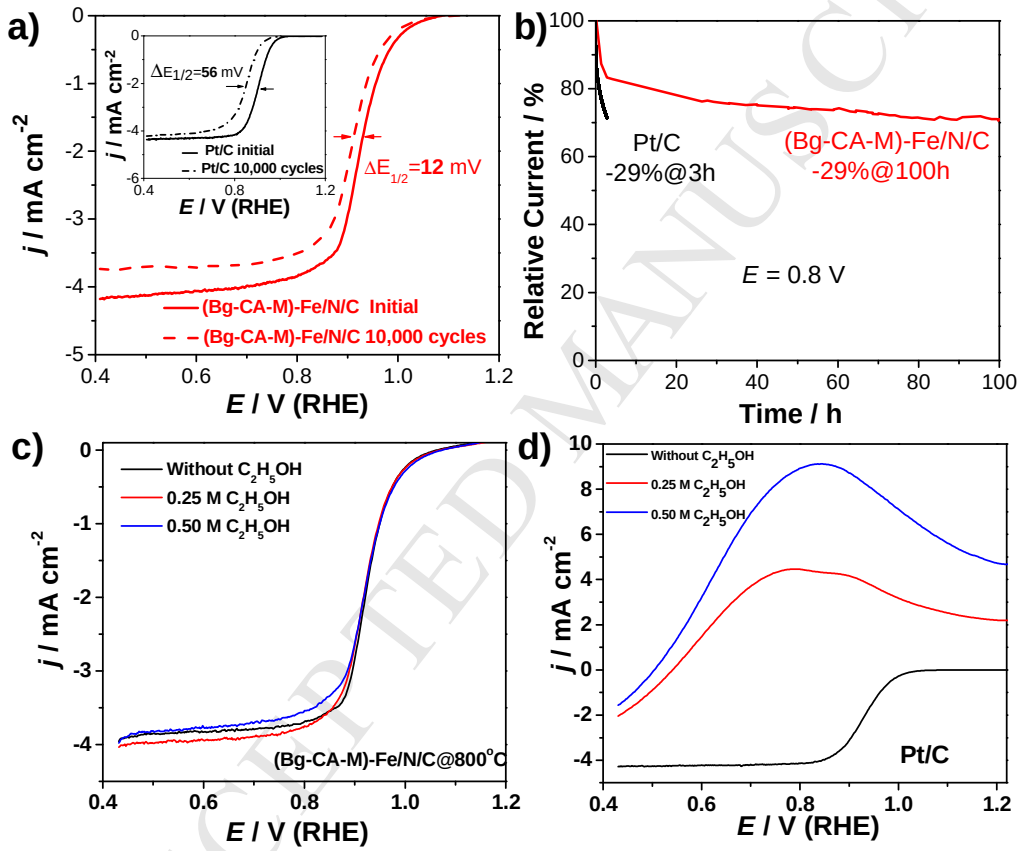

Fig. 8 Stability tests of (Bg-CA-M)-Fe/N/C@800°C and Pt/C catalysts through 10,000 potential cycles between 0.6 and 1.0 V at 50 mV s^{-1} (a) and constant potential at at 0.8 V for 100 h (b) in O_2-saturated 0.1 M NaOH solution; Ethanol tolerance of (Bg-CA-M)-Fe/N/C@800°C (c) and Pt/C catalyst (d) in O_2-saturated 0.1 M NaOH with different concentration of ethanol (0, 0.25, and

0.50 M). Scan rate: 10 mV s^{-1}; Rotating rate: 900 rpm.

(Bg-CA-M)-Fe/N/C@800°C exhibits high alcohol tolerance. The ORR polarization curve recorded in the 0.1 M NaOH is similar to those recorded in 0.1 M NaOH solution containing 0.25 and 0.50 M ethanol (Fig. 8c). That is, ethanol can not influence the ORR on (Bg-CA-M)-Fe/N/C@800°C. The electrooxidation of alcohols involves the breakage of strong C-H bond, which can not be catalyzed by the Fe/N/C catalysts. In contrast, as for the Pt/C, ethanol oxidation current totally overwhelms the oxygen reduction current in 0.1 M NaOH + 0.25 M ethanol solution (Fig. 8d). These results indicate that (Bg-CA-M)-Fe/N/C catalyst has a promising application in DAFCs.

3.5 Performance of alkaline membrane direct ethanol fuel cell

We carried out the tests of alkaline membrane DEFC with (Bg-CA-M)-Fe/N/C@800°C catalyst as cathode for ORR, homemade Pd/C as anode for ethanol oxidation and commercial A-201 alkaline anion exchange membrane. Fig. 9a shows polarization curves and power density plots of alkaline membrane DEFC fed with 2 M ethanol with different concentration of KOH solution. Unlike acidic Nafion-based DEFCs where only ethanol solution is used in the anode, alkaline membrane DEFCs still need additional KOH or NaOH electrolyte to compensate the alkali consumption due to the neutralization reaction between OH^- and ethanol oxidation products (acetic acid and CO_2). As shown in Fig. 9a, the DEFC performance is improved with increasing the KOH concentration (0.1 to 1 M) in the feeding solution. The cell temperature is also an important parameter. Fig. 9b shows

polarization curves and power density plots of alkaline membrane DEFC operated at temperatures of 70-90 °C. The fuel 2 M ethanol+1 M KOH was fed at anode. Due to high tolerance to fuel crossover, the open circuit voltage is up to 0.88 V. The peak power density can approach to 64 mW cm^{-2} at 350 mA cm^{-2} when the DEFC is operated at 90 °C. Our alkaline membrane DEFC performance with (Bg-CA-M)-Fe/N/C@800°C cathode is quite high, even comparable to some literature results with Pt/C cathodes (Table S2) [39, 40]. This result demonstrates the potential application of the (Bg-CA-M)-Fe/N/C@800°C for fuel cells

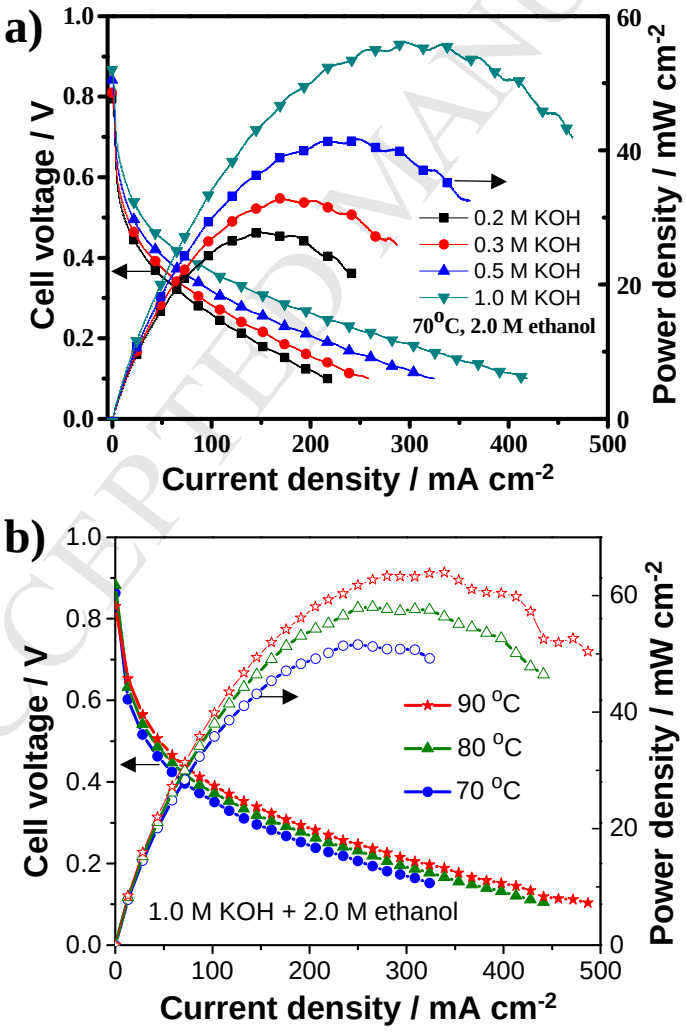

Fig. 9 Polarization curves and power density curves of alkaline membrane direct

ethanol fuel cell with (Bg-CA-M)-Fe/N/C@800^{o}C as cathode catalyst. (a) Effect of KOH concentration from 0.2 to 1.0 M; (b) Effect of cell temperature from 40 to 70°C. A-201 alkaline anion exchange membrane; Anode: 20 wt% Pd/C (2.56 mg_{cat} cm^{-2}); cathode: (Bg-CA-M)-Fe/N/C@800^{o}C (2.56 mg cm^{-2}); O_2: 300 sccm; MEA area: 6.25 cm^2.

4. Conclusions

In conclusion, we prepared bamboo-like nitrogen-doped carbon nanotubes with encapsulated Fe nanoparticles through high-temperature pyrolysis of multiple nitrogen complex of benzoguanamine, cyanuric acid, and melamine. As-prepared (Bg-CA-M)-Fe/N/C catalyst exhibits high ORR activity and low H_2O_2 yield in alkaline medium. The onset potential is up to 1.10 V, and mass activity is 0.578 A g^{-1} at 1.0 V in the alkaline medium. The catalyst also exhibits the high durability and ethanol tolerance. When the (Bg-CA-M)-Fe/N/C is applied in alkaline membrane direct ethanol fuel cell, the peak power density can be as high as 64 mW cm^{-2}. The excellent performance strongly indicates that (Bg-CA-M)-Fe/N/C is promising to replace Pt-based catalysts in alkaline medium.

Acknowledgements. This study was supported by grants from National Key Research and Development Program of China (2016YFB0101202), National Natural Science Foundation of China (21373175, 21361140374, and 21621091), and Fundamental Research Funds for the Central Universities (20720150109).

Refreences:

[1] G. Wu, K. L. More, C. M. Johnston, P. Zelenay, High-performance electrocatalysts for oxygen reduction derived from polyaniline, iron, and cobalt, Science, 332 (2011) 443-447.

[2] H. T. Chung, J. H. Won, P. Zelenay, Active and stable carbon nanotube/nanoparticle composite electrocatalyst for oxygen reduction, Nat. Commun., 4 (2013) 1992.

[3] K. P. Gong, F. Du, Z. H. Xia, M. Durstock, L. M. Dai, Nitrogen-doped carbon nanotube arrays with high electrocatalytic activity for oxygen reduction, Science, 323 (2009) 760-764.

[4] M. Lefevre, E. Proietti, F. Jaouen, J. P. Dodelet, Iron-based catalysts with improved oxygen reduction activity in polymer electrolyte fuel cells, Science, 324 (2009) 71-74.

[5] S. Park, Y. Y. Shao, J. Liu, Y. Wang, Oxygen electrocatalysts for water electrolyzers and reversible fuel cells: status and perspective, Energy Environ. Sci., 5 (11) (2012) 9331-9344.

[6] Y. G. Li, W. Zhou, H. L. Wang, L. M. Xie, Y. Y. Liang, F. Wei, et al., An oxygen reduction electrocatalyst based on carbon nanotube–graphene complexes, Nat. Nanotechnol., 7 (2012) 394-400.

[7] S. Maldonado, K. J. Stevenson, Influence of nitrogen doping on oxygen reduction electrocatalysis at carbon nanofiber electrodes, J. Phys. Chem. B, , 109 (10)

(2005) 4707-4716.

[8] R. L. Liu, D. Q. Wu, X. L. Feng, K. Mullen, Nitrogen-doped ordered mesoporous graphitic arrays with high electrocatalytic activity for oxygen reduction, Angew. Chem. Int. Ed., 49 (14) (2010) 2565-2569.

[9] P. Chen, T. Zhou, L. Xing, K. Xu, Y. Tong, H. Xie, et al., Atomically dispersed iron-nitrogen species as electrocatalysts for bifunctional oxygen evolution and reduction reactions, Angew. Chem. Int. Ed., 56 (2) (2017) 610-614.

[10] W. J. Jiang, L. Gu, L. Li, Y. Zhang, X. Zhang, L.-J. Zhang, et al., Understanding the high activity of Fe-N-C electrocatalysts in oxygen reduction: Fe/Fe_3C nanoparticles boost the activity of $Fe-N_x$, J. Am. Chem. Soc., 138 (10) (2016) 3570-3578.

[11] W. Shi, Y. C. Wang, C. Chen, X. D. Yang, Z. Y. Zhou, S. G. Sun, A mesoporous Fe/N/C ORR catalyst for polymer electrolyte membrane fuel cells, Chin. J. Catal., 37 (7) (2016) 1103-1108.

[12] Y. C. Wang, Y. J. Lai, L. Song, Z. Y. Zhou, J. G. Liu, Q. Wang, et al., S-doping of an Fe/N/C ORR catalyst for polymer electrolyte membrane fuel cells with high power density, Angew. Chem. Int. Ed., 54 (34) (2015) 9907-9910.

[13] Hoon T. Chung, Piotr Zelenay, A simple synthesis of nitrogen-doped carbon micro- and nanotubes, Chem. Commun., 51 (2015) 13546-13549.

[14] P. Zhao, W. Xu, X. Hua, W. Luo, S. Chen, G. Cheng, Facile Synthesis of a N-doped Fe_3C@CNT/porous carbon hybrid for an advanced oxygen reduction and water oxidation electrocatalyst, J. Phys. Chem. C, 120 (20) (2016)

11006-11013.

[15] D. H. Deng, L. Yu, X. Q. Chen, G. X. Wang, L. Jin, X. L. Pan, et al., Iron encapsulated within pod-like carbon nanotubes for oxygen reduction reaction, Angew. Chem. Int. Ed., 52 (2013) 371.

[16] Z. Chen, D. Higgins, Z. Chen, Nitrogen doped carbon nanotubes and their impact on the oxygen reduction reaction in fuel cells, Carbon, 48 (11) (2010) 3057-3065.

[17] M. Rauf, Y. D. Zhao, Y. C. Wang, Y. P. Zheng, C. Chen, X. D. Yang, et al., Insight into the different ORR catalytic activity of Fe/N/C between acidic and alkaline media: Protonation of pyridinic nitrogen, Electrochem. Commun., 73 (2016) 71-74.

[18] G. Zhang, R. Chenitz, M. Lefèvre, S. Sun, J. P. Dodelet, Is iron involved in the lack of stability of Fe/N/C electrocatalysts used to reduce oxygen at the cathode of PEM fuel cells? Nano Energy, 29 (2016) 111-125.

[19] G. Liu, X. Li, P. Ganesan, B.N. Popov, Studies of oxygen reduction reaction active sites and stability of nitrogen-modified carbon composite catalysts for PEM fuel cells, Electrochim. Acta, 55 (8) (2010) 2853-2858.

[20] D. Banham, S. Ye, K. Pei, J.-i. Ozaki, T. Kishimoto, Y. Imashiro, A review of the stability and durability of non-precious metal catalysts for the oxygen reduction reaction in proton exchange membrane fuel cells, J. Power Sources, 285 (2015) 334-348.

[21] C. Chen, X. D. Yang, Z. Y. Zhou, Y. J. Lai, M. Rauf, Y. Wang, et al.,

Aminothiazole-derived N,S,Fe-doped graphene nanosheets as high performance electrocatalysts for oxygen reduction, Chem. Commun., 51 (96) (2015) 17092-17095.

[22] Y. Zheng, Y. Jiao, L. Ge, M. Jaroniec, S.Z. Qiao, Two-step boron and nitrogen doping in graphene for enhanced synergistic catalysis, Angew. Chem. Int. Ed., 52 (11) (2013) 3110-3116.

[23] J. Liu, X. Sun, P. Song, Y. Zhang, W. Xing, W. Xu, High-performance oxygen reduction electrocatalysts based on cheap carbon black, nitrogen, and trace iron, Adv. Mater., 25 (47) (2013) 6879-6883.

[24] B.J. Kim, D.U. Lee, J. Wu, D. Higgins, A. Yu, Z. Chen, Iron- and nitrogen-functionalized graphene nanosheet and nanoshell composites as a highly active electrocatalyst for oxygen reduction reaction, J. Phys. Chem. C, 117 (50) (2013) 26501-26508.

[25] N. Ramaswamy, U. Tylus, Q. Jia, S. Mukerjee, Activity descriptor identification for oxygen reduction on nonprecious electrocatalysts: linking surface science to coordination chemistry, J. Am. Chem. Soc., 135 (41) (2013) 15443-15449.

[26] T. Palaniselvam, V. Kashyap, S.N. Bhange, J.-B. Baek, S. Kurungot, Nanoporous graphene enriched with Fe/Co-N active sites as a promising oxygen reduction electrocatalyst for anion exchange membrane fuel cells, Adv. Funct. Mater., 26 (13) (2016) 2150-2162.

[27] J. Pan, C. Chen, Y. Li, L. Wang, L. Tan, G. Li, et al., Constructing ionic highway in alkaline polymer electrolytes, Energy Environ. Sci, 7 (1) (2014) 354-360.

[28] S. Gu, J. Skovgard, Y.S. Yan, Engineering the Van der Waals interaction in cross-linking-free hydroxide exchange membranes for low swelling and high conductivity, ChemSusChem, 5 (5) (2012) 843-848.

[29] L. Zhu, J. Pan, C.M. Christensen, B. Lin, M.A. Hickner, Functionalization of Poly(2,6-dimethyl-1,4-phenylene oxide)s with Hindered Fluorene Side Chains for Anion Exchange Membranes, Macromolecules, 49 (9) (2016) 3300-3309.

[30] Y. C. Wang, L. Huang, P. Zhang, Y. T. Qiu, T. Sheng, Z. Y. Zhou, et al., Constructing a triple-phase interface in micropores to boost performance of Fe/N/C catalysts for direct methanol fuel cells, ACS Energy Lett., 2 (3) (2017) 645-650.

[31] A. Dutta, J. Datta, Energy efficient role of Ni/NiO in PdNi nano catalyst used in alkaline DEFC, J. Mater. Chem. A, 2 (9) (2014) 3237-3250.

[32] Y. Qiu, J. Huo, F. Jia, B.H. Shanks, W. Li, N- and S-doped mesoporous carbon as metal-free cathode catalysts for direct biorenewable alcohol fuel cells, J. Mater. Chem. A, 4 (1) (2016) 83-95.

[33] Y. Ishida, L. Chabanne, M. Antonietti, M. Shalom, Morphology control and photocatalysis enhancement by the one-pot synthesis of carbon nitride from preorganized hydrogen-bonded supramolecular precursors, Langmuir, 30 (2) (2014) 447-451.

[34] L. Zhang, J. Zhang, D.P. Wilkinson, H. Wang, Progress in preparation of non-noble electrocatalysts for PEM fuel cell reactions, J. Power Sources, 156 (2) (2006) 171-182.

[35] J. Wang, H. H. Wu, D. F. Gao, S. Miao, G. X. Wang, X. H. Bao, High-density iron nanoparticles encapsulated within nitrogen-doped carbon nanoshell as efficient oxygen electrocatalyst for zinc–air battery, Nano Energy, 13 (2015) 387-396.

[36] R. Cao, R. Thapa, H. Kim, X. Xu, M. Gyu Kim, Q. Li, et al., Promotion of oxygen reduction by a bio-inspired tethered iron phthalocyanine carbon nanotube-based catalyst, Nat. Commun., 4 (2013) 2076.

[37] K. Artyushkova, B. Kiefer, B. Halevi, A. Knop-Gericke, R. Schlogl, P. Atanassov, Density functional theory calculations of XPS binding energy shift for nitrogen-containing graphene-like structures, Chem. Commun., 49 (25) (2013) 2539-2541.

[38] G. Zhong, H. Wang, H. Yu, F. Peng, Nitrogen doped carbon nanotubes with encapsulated ferric carbide as excellent electrocatalyst for oxygen reduction reaction in acid and alkaline media, J. Power Sources, 286 (2015) 495-503.

[39] L. Osmieri, R. Escudero-Cid, M. Armandi, A. H. A. Monteverde Videla, J. L. Garcia Fierro, P. Ocon, et al., Fe-N/C catalysts for oxygen reduction reaction supported on different carbonaceous materials. Performance in acidic and alkaline direct alcohol fuel cells, Appl. Catal. B: Environ., 205 (2017) 637-653.

[40] H. Hou, G. Sun, R. He, Z. Wu, B. Sun, Alkali doped polybenzimidazole membrane for high performance alkaline direct ethanol fuel cell, J. Power Sources, 182 (1) (2008) 95-99.